APPLIED PHYSICS

Magneto-optical chiral metasurfaces for achieving polarization-independent nonreciprocal transmission

Wenjia Li[1,2,3]†, Qingdong Yang[1]†, Oubo You[1]†, Cuicui Lu[1,4], Fuxin Guan[1], Jianlong Liu[2,3]*, Jinhui Shi[2,3]*, Shuang Zhang[1,5,6]*

Nonreciprocal transmission, resulting from the breaking of Lorentz reciprocity, plays a pivotal role in nonreciprocal communication systems by enabling asymmetric forward and backward propagations. Metasurfaces endowed with nonreciprocity represent a compact and facile platform for manipulating electromagnetic waves in an unprecedented manner. However, most passive metasurfaces that achieve nonreciprocal transmissions are polarization dependent. While incorporation of active elements or nonlinear materials can achieve polarization-independent nonreciprocal metasurfaces, the complicated configurations limit their practical applications. To address this issue, we propose and demonstrate a passive and linear metasurface that combines magneto-optical and chiral effects, enabling polarization-independent isolation. The designed metasurface achieves a transmittance of up to 80%, with a high contrast between forward and backward propagations. Our work introduces a novel mechanism for nonreciprocal transmission and lays the foundation for the development of compact, polarization-insensitive nonreciprocal devices.

INTRODUCTION

Metasurfaces are thin structured surfaces capable of manipulating the phase, amplitude, and polarization state of electromagnetic waves in a compact form (*1*–*7*). In recent years, there has been increasing interest in nonreciprocal metasurfaces due to their potential for various applications, including optical isolators (*8*, *9*), directional amplifiers (*10*), and phase shifters (*11*). Various methods have been used to achieve nonreciprocal metasurfaces, such as the magneto-optic effect (*12*–*16*), optical nonlinearity (*17*–*19*), time modulation systems (*20*–*24*), and transistor loading (*25*–*28*). In addition, magnetic meta-atoms have been recently investigated as a means to achieve nonreciprocal transmission (*29*). However, most experimental demonstrations of nonreciprocal transmission are restricted to specific polarization states for the incident beam (*29*, *30*) or experience nonlinear responses (*31*). While it is possible to realize polarization-independent nonreciprocal metasurfaces based on time modulation, these schemes involve active elements and increase complexity and power consumption (*32*, *33*). Implementations using active elements often requires extra power source and typically involve complex designs, while those using nonlinear materials are dependent on signal intensity. Hence, achieving nonreciprocal metasurfaces for arbitrary polarizations using all-passive and linear approaches would be highly desirable for practical applications.

[1]New Cornerstone Science Laboratory, Department of Physics, The University of Hong Kong, Hong Kong 999077, China. [2]Key Laboratory of Photonic Materials and Devices Physics for Oceanic Applications, Ministry of Industry and Information Technology of China, College of Physics and Optoelectronic Engineering, Harbin Engineering University, Harbin 150000, China. [3]Key Laboratory of In-Fiber Integrated Optics of Ministry of Education, College of Physics and Optoelectronic Engineering, Harbin Engineering University, Harbin 150000, China. [4]Key Laboratory of Advanced Optoelectronic Quantum Architecture and Measurements of Ministry of Education, Beijing Key Laboratory of Nanophotonics and Ultrafine Optoelectronic Systems, School of Physics, Beijing Institute of Technology, Beijing 100081, China. [5]Department of Electrical & Electronic Engineering, The University of Hong Kong, Hong Kong 999077, China. [6]Materials Innovation Institute for Life Sciences and Energy (MILES), HKU-SIRI, Shenzhen 518000, China.
*Corresponding author. Email: liujl@hrbeu.edu.cn (J.L.); shijinhui@hrbeu.edu.cn (J.S.); shuzhang@hku.hk (S.Z.)
†These authors contributed equally to this work.

Here, we experimentally demonstrate nonreciprocal transmission for arbitrarily polarized incidences using an all-passive and linear metasurface composed of periodically arranged magneto-optical and chiral (MOC) elements. This polarization-independent nonreciprocal functionality arises from the combination of different cross-polarization conversion behaviors of magneto-optical meta-atoms and chiral meta-atoms, which break time-reversal symmetry and mirror symmetry, respectively. The nonreciprocal metasurface exhibits transmittance above 80% in the forward direction but a much lower transmittance in the backward direction.

RESULTS

Design of MOC metasurface

For a passive and lossless system, the scattering matrix must be unitary, in accordance with conservation of energy. Our goal is to achieve polarization-independent unidirectional transmission, which means that at least all the linear polarization states should exhibit the same responses. To achieve this, the structure should have n-fold rotational symmetry where $n \geq 3$, which leads to decoupling between left circularly polarized (LCP) and right circularly polarized (RCP) channels (*34*). If the system only has zeroth diffraction order, for each of the LCP and RCP channels, then the scattering matrix belongs to U(2) group and has the following general form

$$S = \begin{pmatrix} a & b \\ -e^{i\varphi}b^* & e^{i\varphi}a^* \end{pmatrix} \quad (1)$$

where $|a|^2 + |b|^2 = 1$. According to Eq. 1, the explicit expressions for transmission coefficients in the forward and backward directions are $-e^{-i\varphi}b^*$ and b, respectively. Therefore, they have the same amplitude but they differ only in phase. If one aims to achieve asymmetric transmission in terms of amplitude, then material loss must be introduced into the system or additional diffraction orders must be introduced to provide more channels to the scattering matrix. In our work, we opt for the latter approach to avoid involving material loss. We design a grating structure with a periodicity greater than the free space wavelength, as depicted in Fig. 1. The grating is designed in

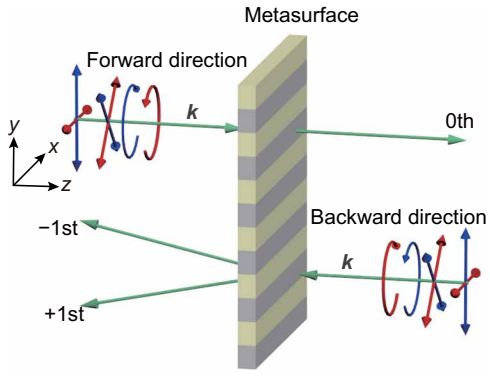

Fig. 1. Schematic of the polarization-independent nonreciprocal transmission. The incident light in the forward direction is entirely transmitted through the zeroth diffraction order, while the incident light in the backward direction is completely transmitted through the positive and negative first diffraction orders.

such a way that, when waves propagate in the forward direction, they transmit through the grating into the zeroth order. On the other hand, during backward propagation, the power is directed into higher diffraction orders, such as positive first and negative first orders.

Breaking the time-reversal symmetry is crucial to achieve nonreciprocal responses in the aforementioned grating configuration. In addition, to ensure polarization-independent responses, subunits with rotational symmetry are necessary so that all linear polarization states exhibit the same responses. There are multiple options for a system to have broken time-reversal symmetry. These include gyroelectric or gyromagnetic responses, which correspond to permittivity (ε) or permeability (μ) tensor with imaginary off-diagonal elements, respectively. In addition, Tellegen and moving media can also be used, involving cross-coupling between electric and magnetic responses (*35*–*37*).

It is well established that Tellegen materials introduce nonreciprocal responses in reflection rather than transmission (*38*), so Tellegen response is not considered for the construction of nonreciprocal metasurfaces. One can use a moving medium to achieve nonreciprocal transmission. A moving medium exhibits different transmission phases in the forward and backward directions, independent of the incident polarization (*35*). To implement this, a grating can be designed with an alternating arrangement of a moving medium and a normal dielectric material. Careful engineering of the grating is necessary so that, in the forward direction, the light transmitting through the moving medium region interferes constructively with that of the normal dielectric region, while in the backward direction, destructive interference occurs. The detailed explanation can be found in the Supplementary Materials (section S1). However, it is important to note that the phase difference of the moving medium in the forward and backward directions is typically extremely small, unless the velocity reaches relativistic values.

In contrast, gyroelectric and gyromagnetic responses are readily available at microwave and terahertz frequencies (*39*–*44*). These responses can both induce polarization rotation in transmission for incident waves of linear polarizations. In the following, we show that grating designed based on the combination of gyromagnetic materials with chiral materials can enable nonreciprocal transmission in terms of amplitude for all polarizations.

Our design is schematically shown in Fig. 2. The designed metasurface is a combination of two types of unit cells for forming the grating configuration. The first type is a magneto-optical element biased by a static magnetic field that respects mirror symmetry in the *z* direction but breaks the time-reversal symmetry, while the

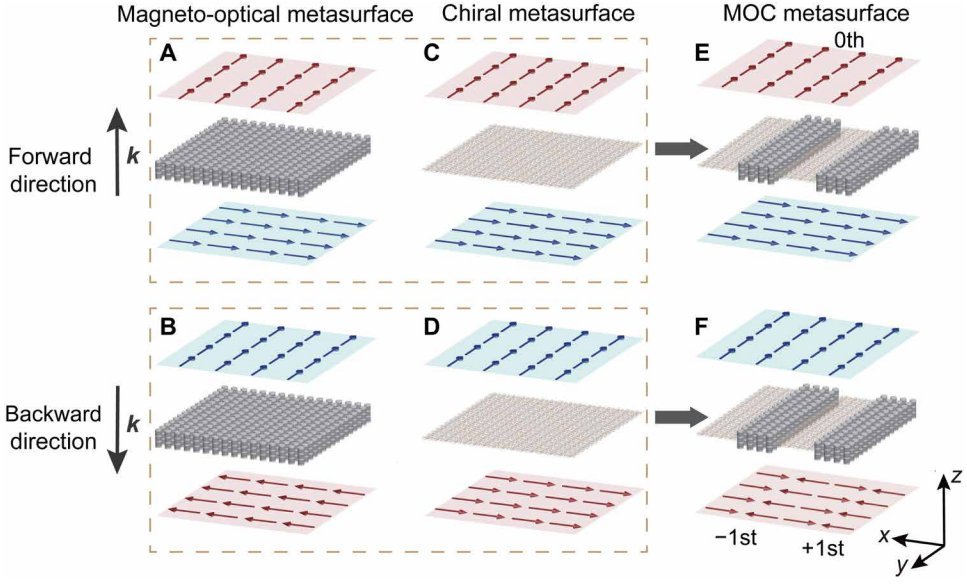

Fig. 2. Illustration of the design of MOC metasurface. For incident wave propagating along the +*z* direction, the (**A**) magneto-optical, (**C**) chiral, and (**E**) MOC metasurfaces rotate −*x* polarization of the incident wave to −*y* polarization in transmission. The MOC metasurface has high transmission in the zeroth diffraction order. For incident wave propagating along the −*z* direction, the (**B**) magneto-optical metasurface rotate −*y* polarization of the incident wave to +*x* polarization in transmission, the (**D**) chiral metasurface rotate −*y* polarization of the incident wave to −*x* polarization in transmission, and as a result, the (**F**) MOC metasurface has zero or very low transmittance in the zeroth diffraction order due to the destructive interference of transmitted waves from the MOC metasurfaces.

second type is a chiral metasurface that lacks any mirror symmetry but respects time-reversal symmetry. Both types of metasurfaces can achieve cross-polarization conversion, but they exhibit different behaviors when the direction of the incident light is reversed.

We first consider a linearly polarized incident wave with electric field oriented along the $-x$ direction is propagating along the $+z$ direction, as shown in Fig. 2A. With judicious design, a metasurface only consisting of the magneto-optical elements can rotate the linear polarization of the incident wave to its cross-polarization in transmission, and without losing generality, we assume that the direction of the bias magnetic field is arranged in a way such that the electric field of the transmitted wave is oriented along the $-y$ direction. When the direction of the incident wave is reversed and the incident electric field is $-y$ polarized, due to the broken time-reversal symmetry, the electric field of the transmitted wave is oriented along the $+x$ direction, as illustrated in Fig. 2B.

Similar to the magneto-optical metasurface, a metasurface only consisting of the chiral elements can also be designed to achieve near-perfect cross-polarization conversion, as demonstrated in Fig. 2 (C and D). The chiral metasurface can be appropriately engineered to rotate the electric field of the incident wave from the $-x$ to $-y$ direction when the incident wave is propagating along the $+z$ direction. However, when the propagation direction of the wave is reversed and the incident electric field is $-y$ polarized, using a simple argument based on the combination of time-reversal symmetry and rotational symmetry, it can be deduced that the E field of the transmitted wave would be rotated to the $-x$ direction.

Next, we consider a MOC metasurface made from periodic arrangement of two stripes that consist of MOC unit cells, as depicted in Fig. 2 (E and F). When a plane wave is incident onto the MOC metasurface along the $+z$ direction, the transmitted waves from the two regions have the same orientation of electric field and interfere constructively, leading to high transmission in the zeroth diffraction order. However, when the direction of incident wave is reversed, there would be a destructive interference due to the opposite orientation of the electric field of the transmitted waves, leading to very low transmittance in the zeroth diffraction order. Note that the same analysis also applies to an incident wave of y polarization. Because waves of arbitrary polarization states can always be decomposed into x and y orientations, the MOC metasurface can, in principle, operate for all incident polarizations.

Design of MOC unit cells

We next discuss the design of the building blocks for the MOC metasurfaces. The magneto-optical unit cell consists of a column stacking of magnet disks and yttrium iron garnet (YIG) ferrite disks in the sequence of *ABABABA*, where *A* represents magnet disk and *B* represents YIG disk. The composite columns are subsequently inserted into a square lattice of circular holes perforated into a dielectric slab, as shown in Fig. 3A. The effective permittivity of YIG disks is 14.5, and the effective permittivity of the dielectric slab is 2.15. The permeability tensor of YIG has nonzero off-diagonal components, and the detailed parameters are provided in Materials and Methods. Besides providing the bias magnetic field, the magnet disks coated with metal film function as perfect electric conductors. The neighboring pair of magnet disks forms a resonance cavity, which can strongly enhance the magnetic field of the incident wave inside the YIG disk sandwiched in between, as illustrated by the simulation results shown in Fig. 3B. As a result, the magneto-optical effect is strongly enhanced, and the magneto-optical metasurface works as an effective Faraday rotator, which has the ability to rotate the polarization for transmitted wave. The influence of the magnet disks on the polarization conversion and the magnetic field distribution within the structure is analyzed in the Supplementary Materials (section S2). The simulated amplitudes of the transmitted electric fields for the magneto-optical metasurfaces, for an incident x-polarized wave, are depicted in Fig. 3D. The subscripts "f" and "b" represent forward and backward transmissions, respectively. The superscripts "co" and "cross" denote the co-polarization and cross-polarization of the transmitted wave relative to the incident wave, respectively. The simulation shows that the amplitude of the cross-polarized transmission can be maintained above 0.9 in the frequency range of 8.25 to 8.95 GHz.

The conjugated gammadion structure made from copper is chosen as the chiral element (*45*, *46*) for realizing orthogonal polarization conversion. A metasurface consisting of such chiral structures sandwiched between three dielectric layers of the same thickness, as illustrated in Fig. 3C, can generate a strong chiral optical effect due to the lack of mirror symmetry and the strong coupling between the top and bottom layers. This leads to nearly complete conversion of the incident wave to the orthogonally polarized state in transmission at the resonance frequency around 8.95 GHz, as shown in Fig. 3E.

Simultaneously achieving high transmitted amplitudes with both MOC elements is beneficial for attaining optical isolation. Moreover, the phases of transmission through these two types of elements plays a crucial role for attaining optical isolation as they directly influence the superposition of the transmitted fields. By carefully designing the geometries of the two elements, the simulated phases of the transmitted field with cross-polarization for the two metasurfaces are in phase for forward propagation but π out of phase for backward propagation, near the frequency of 8.95 GHz, as illustrated in Fig. 3 (F and G). This implies that a notable isolation effect can be achieved around this frequency with the designed MOC metasurface.

Numerical simulation of the MOC metasurface

A MOC metasurface is formed by combining chiral elements and magneto-optical elements arranged in a periodic pattern, as shown in Fig. 2. Each supercell of the MOC metasurface consists of four chiral elements and four magneto-optical elements. The simulated transmittances of the MOC metasurfaces with varying numbers of MOC units are provided in the Supplementary Materials (section S3). The transmittance refers to the intensity ratio of the transmitted and incident electric fields. The period of the MOC metasurface along the x direction is eight times that of the aforementioned chiral metasurface and magneto-optical metasurface. The simulated transmittances of the MOC metasurface for x linearly polarized, y linearly polarized, RCP, and LCP incidences are presented in Fig. 4 (A to D), respectively. The first and second superscripts correspond to the transmitted and incident polarization states, respectively. The superscripts "x," "y," "+," "−," "R," and "L" denote the x, y, +45°, −45°, RCP, and LCP states, respectively. The transmittances of the forward and backward propagations are markedly different at the frequency of 8.9 GHz (Fig. 4, A and B). The transmitted light is predominantly converted to the cross-polarization under both x- and y-polarized incidences, which is consistent with the analysis based on the interference of light transmitting through the two different types of elements. The

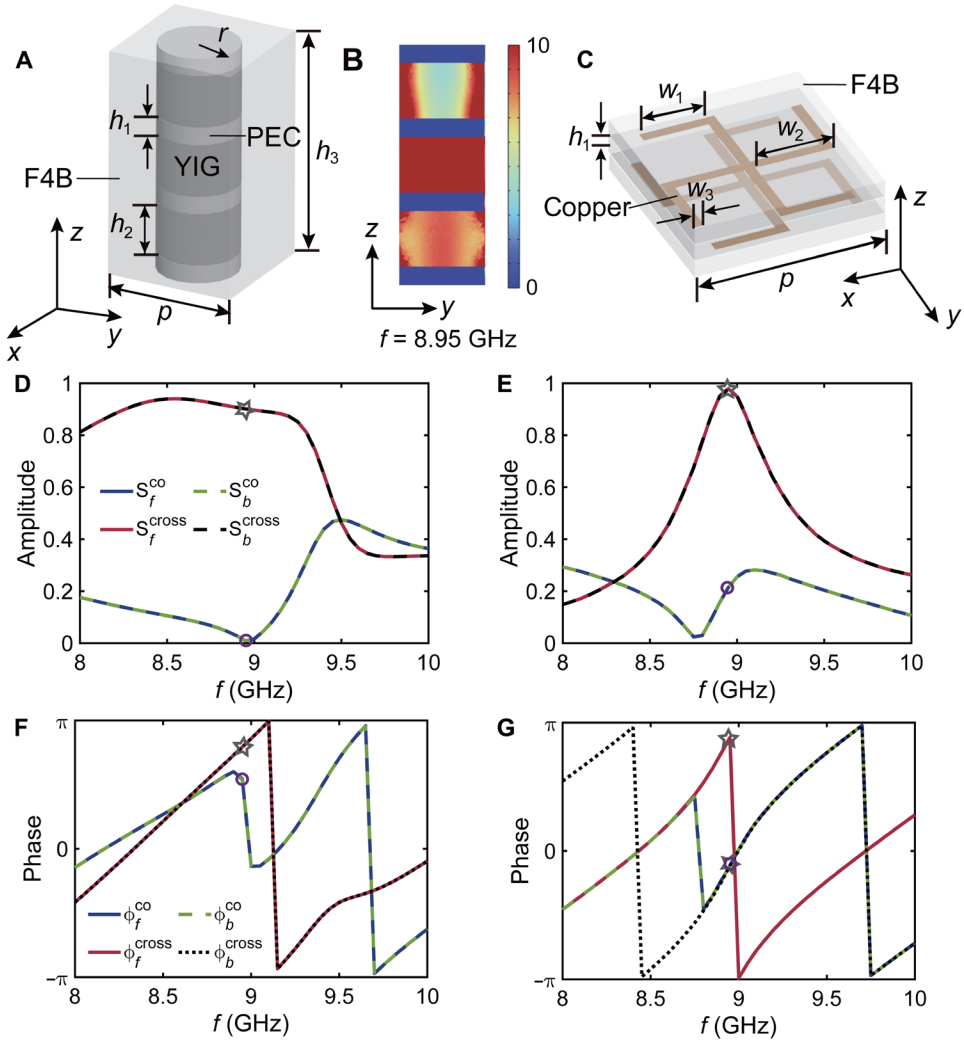

Fig. 3. Design of the MOC unit cells. (**A**) Schematic of the magneto-optical unit cell. The magnet and YIG disks have the same radius $r = 2.3$ mm. The heights of magnet disk [coated with metal which can be regarded as perfect electric conductor (PEC)], YIG disk, and polytetrafluoroethylene and glass fibre (F4B) dielectric slab are $h_1 = 1$ mm, $h_2 = 3$ mm and $h_3 = 13$ mm, respectively. (**B**) The magnetic field distribution within the magneto-optical unit cell at the frequency of 8.95 GHz shows a strong enhancement in the YIG layers. (**C**) Schematic of the chiral unit cell. The geometric parameters of the chiral structure are $w_1 = 3.1$ mm, $w_2 = 2.5$ mm, and $w_3 = 0.4$ mm. The chiral structure has a thickness of 70 μm. The period of the MOC unit cells is $p = 7.4$ mm. The simulated amplitudes of the transmitted electric fields for the (**D**) magneto-optical and (**E**) chiral metasurfaces with incidence of an *x*-polarized wave are shown. The simulated phases of the transmitted field with cross-polarization for the (**F**) magneto-optical and (**G**) chiral metasurfaces are shown.

peaks of transmittance reach 87.4 and 87.3% for *x*- and *y*-polarized incidences, respectively, with the maximum ratios between the transmittances in opposite directions approaching 41.3 and 38.9. The simulated electric field distributions for forward propagation under the *x*-polarized incidence and for backward propagation under *y*-polarized incidence at the frequency of 8.9 GHz are presented in Fig. 4 (C and D), respectively. The *x*-polarized light is converted to the *y*-polarized light for forward propagation; the *y*-polarized light is converted to the *x*-polarized light for backward propagation. It is worth noting that the period of the designed MOC metasurface is larger than the wavelength of the incident light, and first-order diffractions exist. In the forward direction, the transmitted wave remains nearly a plane wave, confirming that nearly all the energy is directed into the zeroth order. In contrast, the transmitted light primarily deflects to the positive and negative first-order diffraction for the backward propagation, as indicated by the interference pattern. The ideal transmission matrices of the forward and backward incidences are given in the Supplementary Materials (section S4).

The simulated transmittances of the MOC metasurface for the incident polarization direction of ±45° with respect to the *x* axis are shown in Fig. 4 (E and F), respectively. The peaks of transmittance reach 87.1 and 89.5% for +45° and −45° polarized incidences, respectively. In addition, the transmittance ratios in opposite directions are 58.0 and 29.7 at the frequency of 8.9 GHz. Under illumination of circularly polarized waves, the MOC metasurface largely preserves the handedness of transmitted wave. This is due to the fourfold rotational symmetry of the individual constitutive elements despite the fact that the rotation symmetry is broken at the supercell level. Consequently, both RCP and LCP waves exhibit high co-polarization transmittance

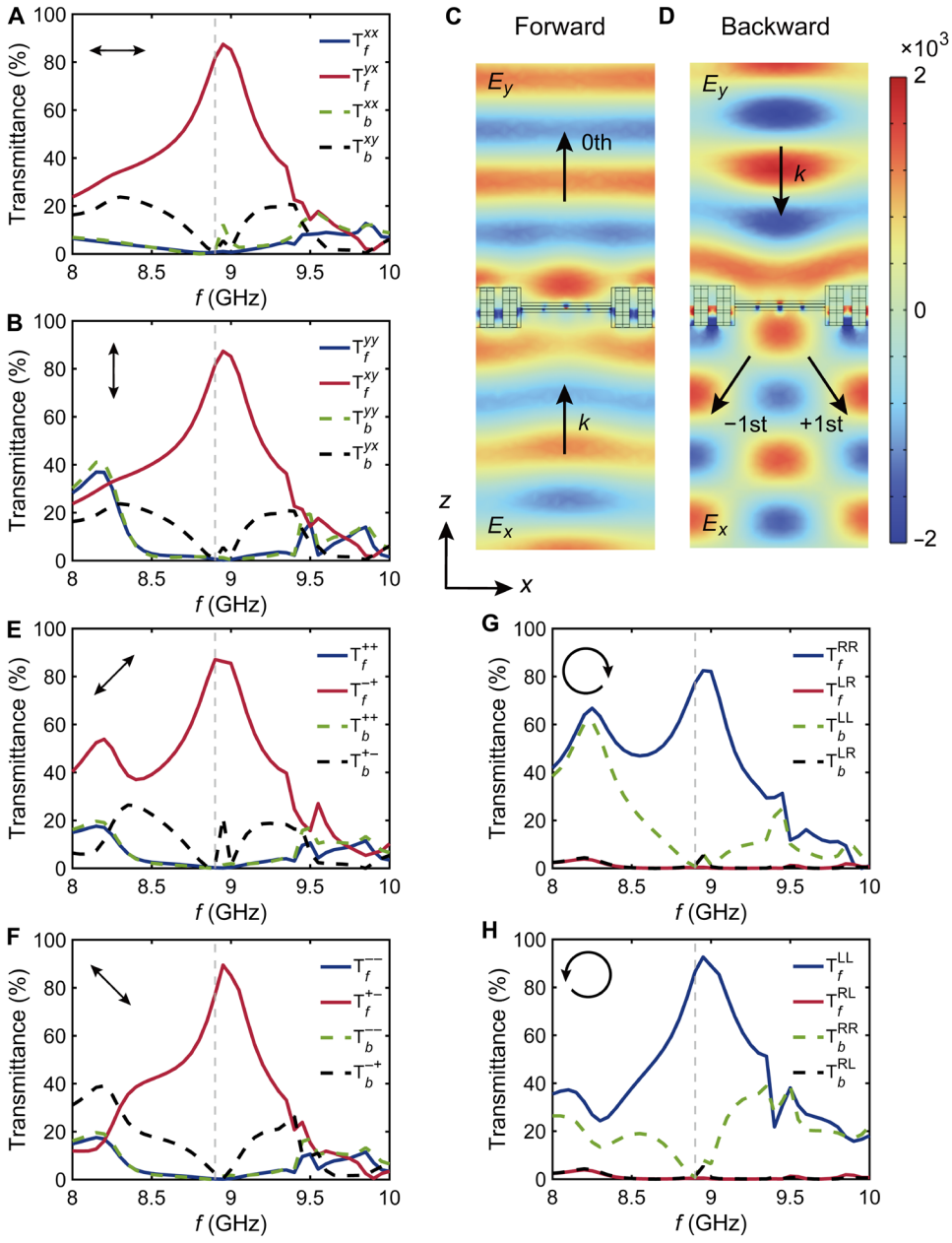

Fig. 4. Numerical results of the MOC metasurface. (**A** and **B**) Simulated transmittances of the MOC metasurface for *x* linearly and *y* linearly polarized incidences, respectively. Field distributions of E_y for the (**C**) forward under *x*-polarized incidence and (**D**) backward propagations under *y*-polarized incidence at the frequency of 8.9 GHz are shown. (**E** to **H**) Simulated transmittances of the MOC metasurface for +45° linearly polarized, −45° linearly polarized, RCP, and LCP incidences, respectively.

for forward propagation at the frequency of 8.9 GHz, as shown in Fig. 4 (G and H). The peaks of the simulated transmittance reach 82.5 and 92.7% for RCP and LCP incidences, respectively. The maximum transmittance ratios for opposite propagations are 38.0 and 42.1 for RCP and LCP incidences, respectively.

Observation of polarization-independent nonreciprocal transmission

To validate the optical isolation performances, the proposed metasurface is fabricated and transmission measurements are conducted using an R&S ZNA43 vector network analyzer (VNA). The top view and front view of the MOC metasurface are depicted in Fig. 5 (A and B), respectively. Two standard linearly polarized horn antennas are positioned on both sides of the metasurface to transmit and receive signals. The measured transmittances of the MOC metasurface for *x*-polarized and *y*-polarized incidences are shown in Fig. 5 (C and D), respectively. The measured transmission peaks are slightly lower than the numerical results, but they still achieve a large value of 82%, while the measured transmittance ratios between the opposite propagation directions are 31.6 and 21.7 for the two types of incidences at a frequency of 9.25 GHz. In the experiments, factors such as the magnetic field of YIG materials, the gap between chiral

and dielectric layers, finite metasurface sizes, material losses, and measurement errors may contribute to discrepancies between experimental and simulated results. The measured amplitudes of the transmitted electric fields for the MOC metasurfaces with an incident *y*-polarized wave are presented in the Supplementary Materials (section S5). The calculated transmittances of the MOC metasurface from the measured data of the two metasurface types are consistent with the measured results of the MOC metasurface in Fig. 5D.

We further characterize the nonreciprocal unidirectional transmission for other polarization states of the incident light. The transmittance of the MOC metasurface is measured for +45° and −45° polarized incidences, as illustrated in Fig. 5 (E and F). The peak transmittances are observed to be 82 and 84.5% for the two incidences, respectively. The maximum transmittance ratios for the opposite propagations are found to be 36.8 and 21.3 for the two types of incidences. The transmittance of the MOC metasurface for RCP and LCP incidences can be determined by combining the measured results for *x*-polarized and *y*-polarized incidences, as depicted in Fig. 5 (G and H), respectively, with the method described in the Supplementary Materials (section S6). The results demonstrate a notable optical isolation performance that are consistent with the simulated results (Fig. 4, G and H). The peak transmittances reach 81.1 and 85.5% for the RCP and LCP incidences, respectively, with the transmittance ratios reaching 20.3 and 37.8 at a frequency of 9.25 GHz. The discrepancy in circularly polarized responses between simulation and experiment is mainly due to the difference in the static magnetic field of YIG materials. While the simulation assumes a uniform field, the actual field in the experiment may vary and be nonuniform.

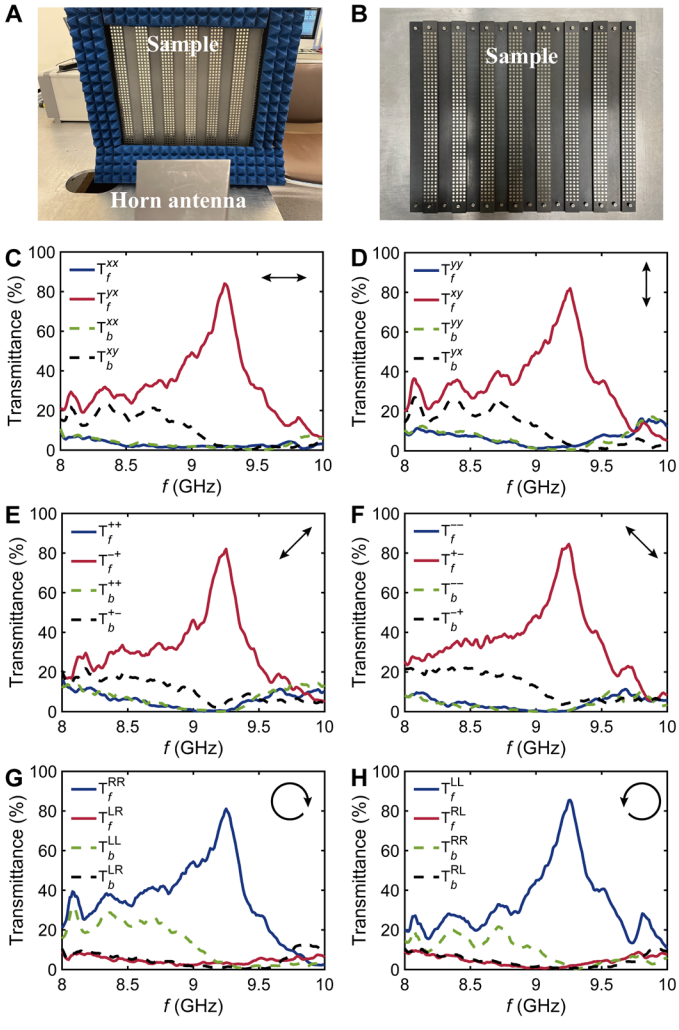

Fig. 5. Nonreciprocal transmission experiments of the MOC metasurface. (**A**) Experimental setup for the measurement of transmission. (**B**) Front view of the MOC metasurface. (**C** to **F**) Measured transmittances of *x*-polarized, *y*-polarized, +45° polarized, and −45° polarized incidences, respectively. (**G** and **H**) Calculated transmittances of RCP and LCP incidences.

DISCUSSION

We have demonstrated polarization-independent nonreciprocal transmission using a MOC metasurface. The nonreciprocal performance arises from the combination of chiral and magneto-optical elements, which display distinct cross-polarization conversion characteristics by breaking mirror symmetry and time-reversal symmetry, respectively. The incorporation of the magnets into the metasurface design not only provides the local bias dc magnetic field but also forms a magnetically resonant cavity that greatly enhances the interaction of the incident electromagnetic wave with the gyromagnetic material. Considering the polarization-independent nonreciprocal functionalities of the magneto-optical metasurface, it can be applied to a nonreciprocal cylindrical metalens, as provided in the Supplementary Materials (section S7). Benefiting from their capability to achieve optical isolation in electromagnetic systems in a compact platform, the MOC metasurfaces are expected to have a broad range of applications such as unidirectional screens, illusion cloaks, nonreciprocal wireless communication, and radar systems.

MATERIALS AND METHODS

Numerical simulations

The numerical simulation was conducted using the commercial software COMSOL Multiphysics. The simulated transmission spectra and electric field distributions were acquired by illuminating a plane wave source with scanning frequencies. The plane wave source with the propagation direction along the *z* axis is set in a port, and the transmitted field is recorded in the opposite port. For the unit cell simulations, the boundaries are set to be periodic along the *x* and *y* axes. The scattering boundaries are used along the *z* axis.

The relative permeability tensor of YIG materials is given by

$$\mu = \begin{pmatrix} \mu_1 & i\kappa & 0 \\ -i\kappa & \mu_1 & 0 \\ 0 & 0 & \mu_2 \end{pmatrix}, \text{where } \kappa = \frac{\omega_m \omega}{(\omega_0 + i\alpha\omega)^2 - \omega^2}, \mu_1 = 1 + \frac{\omega_m(\omega_0 + i\alpha\omega)}{(\omega_0 + i\alpha\omega)^2 - \omega^2}, \mu_2 = 1$$

$\omega_m = \gamma 4\pi M_s$, $\omega_0 = \gamma H_0$, $\alpha = 0.0088$ is the damping coefficient, ω is the operation frequency, $\gamma = 2.8$ MHz/Oe is the gyromagnetic ratio, $4\pi M_s = 1780$ Oe is the saturation magnetization, and $H_0 = 1600$ Oe is the static magnetic field along the *z* direction.

Experimental validation

The proposed dielectric slabs and chiral metasurface are fabricated using the printed circuit board technique on an RT 5880 substrate. The MOC metasurface consists of eight periods in the *x* direction and six periods in the *y* direction. The period of the MOC metasurface is combined by four magneto-optical elements

and chiral elements staggered periodically. YIG disks and magnet disks are inserted at the holes of the dielectric slabs interchangeably. The metasurfaces are surrounded by absorbers to avoid unwanted scattering. The transmission coefficients are measured by a R&S ZNA43 VNA. The two linearly polarized horn antennas are connected to port 1 and port 2 of the VNA for the measurement of the transmission coefficients. Without any postprocessing, the measured transmission amplitude and phase are recorded to demonstrate the experimental results.

Supplementary Materials

This PDF file includes:

Supplementary Text
Table S1
Figs. S1 to S5

REFERENCES AND NOTES

1. G. X. Zheng, H. Muhlenbernd, M. Kenney, G. X. Li, T. Zentgraf, S. Zhang, Metasurface holograms reaching 80% efficiency. *Nat. Nanotechnol.* **10**, 308–312 (2015).
2. X. B. Yin, Z. L. Ye, J. Rho, Y. Wang, X. Zhang, Photonic spin Hall effect at metasurfaces. *Science* **339**, 1405–1407 (2013).
3. G. X. Li, S. M. Chen, N. Pholchai, B. Reineke, P. W. H. Wong, E. Y. B. Pun, K. W. Cheah, T. Zentgraf, S. Zhang, Continuous control of the nonlinearity phase for harmonic generations. *Nat. Mater.* **14**, 607–612 (2015).
4. Y. Chen, H. C. Deng, X. B. Sha, W. J. Chen, R. Z. Wang, Y. H. Chen, D. Wu, J. R. Chu, Y. S. Kivshar, S. M. Xiao, C. W. Qiu, Observation of intrinsic chiral bound states in the continuum. *Nature* **613**, 474–478 (2023).
5. X. D. Zhang, Y. L. Liu, J. C. Han, Y. Kivshar, Q. H. Song, Chiral emission from resonant metasurfaces. *Science* **377**, 1215–1218 (2022).
6. A. M. Shaltout, V. M. Shalaev, M. L. Brongersma, Spatiotemporal light control with active metasurfaces. *Science* **364**, eaat3100 (2019).
7. A. H. Dorrah, F. Capasso, Tunable structured light with flat optics. *Science* **376**, eabi6860 (2022).
8. D. Jalas, A. Petrov, M. Eich, W. Freude, S. Fan, Z. Yu, R. Baets, M. Popović, A. Melloni, J. D. Joannopoulos, M. Vanwolleghem, C. R. Doerr, H. Renner, What is—and what is not—an optical isolator. *Nat. Photonics* **7**, 579–582 (2013).
9. Z. Yu, S. Fan, Complete optical isolation created by indirect interband photonic transitions. *Nat. Photonics* **3**, 91–94 (2009).
10. E. Galiffi, P. A. Huidobro, J. B. Pendry, Broadband nonreciprocal amplification in luminal metamaterials. *Phys. Rev. Lett.* **123**, 206101 (2019).
11. X. Wang, A. Díaz-Rubio, H. Li, S. A. Tretyakov, A. Alù, Theory and design of multifunctional space-time metasurfaces. *Phys. Rev. Appl.* **13**, 044040 (2020).
12. W. C. Wong, W. Y. Wang, W. T. Yau, K. H. Fung, Topological theory for perfect metasurface isolators. *Phys. Rev. B* **101**, 121405 (2020).
13. B. Fan, M. E. Nasir, L. H. Nicholls, A. V. Zayats, V. A. Podolskiy, Magneto-optical metamaterials: Nonreciprocal transmission and Faraday effect enhancement. *Adv. Opt. Mater.* **7**, 1801420 (2019).
14. F. R. Prudencio, M. G. Silveirinha, Optical isolation of circularly polarized light with a spontaneous magnetoelectric effect. *Phys. Rev. A* **93**, 043846 (2016).
15. A. B. Khanikaev, S. H. Mousavi, G. Shvets, Y. S. Kivshar, One-way extraordinary optical transmission and nonreciprocal spoof plasmons. *Phys. Rev. Lett.* **105**, 126804 (2010).
16. W. Y. Wang, W. T. Yau, Y. X. Cui, J. Wang, K. H. Fung, Maxwell's demon-like nonreciprocity by non-Hermitian gyrotropic metasurfaces. *Phys. Rev. Res.* **3**, L022006 (2021).
17. B. Y. Jin, C. Argyropoulos, Self-induced passive nonreciprocal transmission by nonlinear bifacial dielectric metasurfaces. *Phys. Rev. Appl.* **13**, 054056 (2020).
18. M. Lawrence, D. R. Barton, J. A. Dionne, Nonreciprocal flat optics with silicon metasurfaces. *Nano Lett.* **18**, 1104–1109 (2018).
19. A. M. Mahmoud, A. R. Davoyan, N. Engheta, All-passive nonreciprocal metastructure. *Nat. Commun.* **6**, 8359 (2015).
20. X. Wang, J. Q. Han, S. C. Tian, D. X. Xia, L. Li, T. J. Cui, Amplification and manipulation of nonlinear electromagnetic waves and enhanced nonreciprocity using transmissive space-time-coding metasurface. *Adv. Sci.* **9**, 2105960 (2022).
21. X. Wang, G. Ptitcyn, V. S. Asadchy, A. Diaz-Rubio, M. S. Mirmoosa, S. H. Fan, S. A. Tretyakov, Nonreciprocity in bianisotropic systems with uniform time modulation. *Phys. Rev. Lett.* **125**, 266102 (2020).
22. L. Zhang, X. Q. Chen, R. W. Shao, J. Y. Dai, Q. Cheng, G. Castaldi, V. Galdi, T. J. Cui, Breaking reciprocity with space-time-coding digital metasurfaces. *Adv. Mater.* **31**, e1904069 (2019).
23. J. W. Zang, A. Alvarez-Melcon, J. S. Gomez-Diaz, Nonreciprocal phased-array antennas. *Phys. Rev. Appl.* **12**, 054008 (2019).
24. D. L. Sounas, A. Alu, Non-reciprocal photonics based on time modulation. *Nat. Photonics* **11**, 774–783 (2017).
25. D. L. Sounas, T. Kodera, C. Caloz, Electromagnetic modeling of a magnetless nonreciprocal gyrotropic metasurface. *IEEE Trans. Antennas Propag.* **61**, 221–231 (2013).
26. T. Kodera, D. L. Sounas, C. Caloz, Magnetless nonreciprocal metamaterial (MNM) technology: Application to microwave components. *IEEE Trans. Micro. Theory Tech.* **61**, 1030–1042 (2013).
27. Z. Y. Wang, Z. Wang, J. Y. Wang, B. Zhang, J. T. Huangfu, J. D. Joannopoulos, M. Soljacic, L. X. Ran, Gyrotropic response in the absence of a bias field. *Proc. Natl. Acad. Sci. U.S.A.* **109**, 13194–13197 (2012).
28. T. Kodera, D. L. Sounas, C. Caloz, Artificial Faraday rotation using a ring metamaterial structure without static magnetic field. *Appl. Phys. Lett.* **99**, 031114 (2011).
29. W. Yang, J. Qin, J. Long, W. Yan, Y. Yang, C. Li, E. Li, J. Hu, L. Deng, Q. Du, L. Bi, A self-biased non-reciprocal magnetic metasurface for bidirectional phase modulation. *Nat. Electron.* **6**, 225–234 (2023).
30. N. Liu, J. Zhao, L. Du, C. Niu, C. Sun, X. Kong, Z. Wang, X. Li, Giant nonreciprocal transmission in low-biased gyrotropic metasurfaces. *Opt. Lett.* **45**, 5917–5920 (2020).
31. A. Tripathi, C. F. Ugwu, V. S. Asadchy, I. Faniayeu, I. Kravchenko, S. Fan, Y. Kivshar, J. Valentine, S. Kruk, Nanoscale optical nonreciprocity with nonlinear metasurfaces. *Nat. Commun.* **15**, 5077 (2024).
32. Q. Ma, L. Chen, H. B. Jing, Q. R. Hong, H. Y. Cui, Y. Liu, L. L. Li, T. J. Cui, Controllable and programmable nonreciprocity based on detachable digital coding metasurface. *Adv. Opt. Mater.* **7**, 1901285 (2019).
33. S. Taravati, B. A. Khan, S. Gupta, K. Achouri, C. Caloz, Nonreciprocal nongyrotropic magnetless metasurface. *IEEE Trans. Antennas Propag.* **65**, 3589–3597 (2017).
34. Q. Yang, W. Chen, Y. Chen, W. Liu, Symmetry protected invariant scattering properties for incident plane waves of arbitrary polarizations. *Laser Photonics Rev.* **15**, 2000496 (2021).
35. Y. Ra'di, V. S. Asadchy, S. A. Tretyakov, One-way transparent sheets. *Phys. Rev. B* **89**, 075109 (2014).
36. A. Degiron, D. R. Smith, One-way glass for microwaves using nonreciprocal metamaterials. *Phys. Rev. E* **89**, 053203 (2014).
37. V. S. Asadchy, A. Díaz-Rubio, S. A. Tretyakov, Bianisotropic metasurfaces: Physics and applications. *Nanophotonics* **7**, 1069–1094 (2018).
38. S. Safaei Jazi, I. Faniayeu, R. Cichelero, D. C. Tzarouchis, M. M. Asgari, A. Dmitriev, S. Fan, V. Asadchy, Optical Tellegen metamaterial with spontaneous magnetization. *Nat. Commun.* **15**, 1293 (2024).
39. P. G. van Engen, K. H. J. Buschow, M. Erman, Magnetic properties and magneto-optical spectroscopy of Heusler alloys based on transition metals and Sn. *J. Magn. Magn. Mater.* **30**, 374–382 (1983).
40. C. Kittel, Theory of the structure of ferromagnetic domains in films and small particles. *Phys. Rev.* **70**, 965–971 (1946).
41. S. Ram, Observation of enhanced dielectric permittivity in Bi^{3+} doped $BaFe_{12}O_{19}$ ferrite. *J. Magn. Magn. Mater.* **80**, 241–245 (1989).
42. K. Haneda, C. Miyakawa, H. Kojima, Preparation of high-coercivity $BaFe_{12}O_{19}$. *J. Am. Ceram. Soc.* **57**, 354–357 (1974).
43. G.-G. Liu, Z. Gao, Q. Wang, X. Xi, Y.-H. Hu, M. Wang, C. Liu, X. Lin, L. Deng, S. A. Yang, P. Zhou, Y. Yang, Y. Chong, B. Zhang, Topological Chern vectors in three-dimensional photonic crystals. *Nature* **609**, 925–930 (2022).
44. M. Shalaby, M. Peccianti, Y. Ozturk, R. Morandotti, A magnetic non-reciprocal isolator for broadband terahertz operation. *Nat. Commun.* **4**, 1558 (2013).
45. R. Zhao, L. Zhang, J. Zhou, T. Koschny, C. M. Soukoulis, Conjugated gammadion chiral metamaterial with uniaxial optical activity and negative refractive index. *Phys. Rev. B* **83**, 035105 (2011).
46. G. Cheng, L. M. Si, P. C. Tang, Q. L. Zhang, X. Lv, Study of symmetries of chiral metasurfaces for azimuth-rotation-independent cross polarization conversion. *Opt. Express* **30**, 5722–5730 (2022).

Acknowledgments

Funding: This work was supported by the New Cornerstone Science Foundation, Research Grants Council of Hong Kong AoE/P-502/20, Research Grants Council of Hong Kong 17309021, Quantum Science Center of Guangdong–Hong Kong–Macao Great Bay Area, National Natural Science Foundation of China 12204126, National Natural Science Foundation of China 12074087, National Natural Science Foundation of China 62275061, and Natural Science Foundation of Heilongjiang Province in China LH2021A008. **Author contributions:** Conceptualization: S.Z. Methodology: S.Z., W.L., and QY. Investigation: W.L., Q.Y., O.Y., C.L., F.G., and J.S. Visualization: W.L. Supervision: S.Z., J.L., and J.S. Writing—original draft: W.L. Writing—review and editing: S.Z., O.Y., J.L., and W.L. **Competing interests:** The authors declare that they have no competing interests. **Data and materials availability:** All data needed to evaluate the conclusions in the paper are present in the paper and/or the Supplementary Materials.

Submitted 3 November 2023
Accepted 26 June 2024
Published 31 July 2024
10.1126/sciadv.adm7458